Journal of Solid State Chemistry **146,** 291–304 (1999)
Article ID jssc.1999.8326, available online at http://www.idealibrary.com on IDEAL®

Perovskite-Type Oxides

I. Structural, Magnetic, and Morphological Properties of $LaMn_{1-x}Cu_xO_3$ and $LaCo_{1-x}Cu_xO_3$ Solid Solutions with Large Surface Area

Piero Porta,*,[1] Sergio De Rossi,* Marco Faticanti,* Giuliano Minelli,* Ida Pettiti,* Luciana Lisi,† and Maria Turco‡

*Centro di Studio del CNR su "Struttura e Attività Catalitica di Sistemi di Ossidi" (SACSO), c/o Dipartimento di Chimica, Università "La Sapienza," Piazzale A. Moro 5, 00185 Rome, Italy; †Istituto di Ricerche sulla Combustione, CNR, Naples, Italy; and ‡Dipartimento di Ingegneria Chimica, Università "Federico II," Naples, Italy

Received October 22, 1998; in revised form March 22, 1999; accepted April 12, 1999

Perovskite-type compounds of general formula $LaMn_{1-x}Cu_xO_3$ and $LaCo_{1-x}Cu_xO_3$ ($x = 0.0$, 0.2, 0.4, 0.6, 0.8, 1.0) were prepared by calcining the citrate gel precursors at 823, 923, and 1073 K. The decomposition of the precursors was followed by thermal analysis and the oxides were investigated by means of elemental analysis (atomic absorption and redox titration), X-ray powder diffraction, BET surface area, X-ray absorption (EXAFS and XANES), electron microscopy (SEM and TEM), and magnetic susceptibility. $LaMn_{1-x}Cu_xO_3$ samples are perovskite-like single phases up to $x = 0.6$. At $x = 0.8$ CuO and La_2CuO_4 phases are present in addition to perovskite. For $x = 1.0$ the material is formed by CuO and La_2CuO_4. Mn(IV) was found by redox titration in all Mn-based perovskite samples, its fraction increasing with the increase in copper content. EXAFS and XANES analyses confirmed the presence of Mn(IV). Cation vacancies in equal amounts in the 12-coordinated *A* and octahedral *B* sites are suggested in the samples with $x = 0.0$ and $x = 0.2$, while for $x = 0.6$ anionic vacancies are present. Materials with sufficiently high surface area (22–36 $m^2 g^{-1}$ for samples fired at 923 K and 14–22 $m^2 g^{-1}$ for those fired at 1073 K) were obtained. Crystallite sizes in the ranges 390–500 and 590–940 Å for samples calcined at 923 and 1073 K, respectively, were determined from the FWHM of the (102) X-ray diffraction peak. TEM patterns of $LaMnO_3$ showed almost regular hexagonal prismatic crystals with sizes of the same order of magnitude (800 Å) of those drawn from X-ray diffraction, while no evidence of defect clustering was drawn out from TEM and electron diffraction images. For the sample with $x = 0.6$, TEM and electron diffraction patterns revealed perturbation of the structure. Magnetic susceptibility studies show a ferromagnetic behavior that decreases with increase in *x*. $LaCo_{1-x}Cu_xO_3$ samples are perovskite-like single phases up to $x = 0.2$. For $x = 0.4$ a small amount of La_2CuO_4, in addition to perovskite, is detected. For $x \geq 0.6$ massive formation of La_2CuO_4 and CuO is observed. Only trivalent cobalt is found by redox titration. Magnetic susceptibility studies have shown that trivalent cobalt is present in all samples as a mixture of paramagnetic Co^{3+} and diamagnetic Co^{III} ions, the Co^{3+} fraction being, at least up to $x = 0.4$, equal to ≈ 0.34. Antiferromagnetic behavior, which increases with increase in *x*, is observed in all $LaCo_{1-x}Cu_xO_3$ samples. $LaCoO_3$ is a stoichiometric perovskite. The substitution of cobalt by Cu^{2+} leads to a positive charge defectivity which is compensated by oxygen vacancies. EXAFS and XANES analyses confirmed the presence of trivalent cobalt. Materials with fairly high surface area (in the ranges 19–27 and 13–21 $m^2 g^{-1}$ for samples calcined at 923 and 1073 K, respectively) were obtained. Crystallite sizes of ≈ 400 and ≈ 1000 Å for samples calcined at 923 and 1073 K, respectively, were determined from the FWHM of the (102) X-ray diffraction peak. Materials with not very clear morphology and crystals with definite structure are distinguishable by SEM for samples calcined at 1073 and at 1273 K, respectively. TEM patterns, for samples calcined at 1073 K, evidence almost regular hexagonal prismatic crystals connected to form "linked structures" and some "spotty crystals," suggesting short-range ordered local defects. For copper-containing samples, calcined at 1273 K, a higher degree of defectivity (probably associated with the interaction of anion vacancies) and the occurrence of "planar faults" are shown by TEM. © 1999 Academic Press

Key Words: solid solution oxide perovskites; La–Mn–Cu perovskites; La–Co–Cu perovskites.

INTRODUCTION

Perovskite-type oxides of general formula ABO_3, where *B* is a cation, usually a transition metal, surrounded by six oxygens in octahedral coordination, and *A* is a cation, usually a rare-earth metal, 12-coordinated by oxygens, which occupies the cavities made by the BO_6 octahedra, have been extensively studied for their physical and technological properties, such as ferroelectricity, piezoelectricity,

[1]To whom correspondence should be addressed. Fax: (0039 6) 490324. E-mail: porta@axrma.uniromal.it.

0022-4596/99 $30.00

piroelectricity, high-temperature superconductivity, magnetic behavior, and catalytic activity (1–3).

Many metallic elements are stable in the perovskite structure provided that the A and B ions have dimensions ($r_A > 0.90$ Å, $r_B > 0.51$ Å) that agree with the limits of the so-called "tolerance factor" t ($0.8 < t < 1.0$) defined by Goldschmidt (4), as $t = (r_A + r_O)/\sqrt{2}(r_B + r_O)$, where r_A, r_B, and r_O are the ionic radii for A, B, and O, respectively.

The partial substitution of A and/or B by other metals with different oxidation state gives rise to a change in the oxidation state (or electronic doping) in the B cation, as in the $La_{1-x}Sr_xMnO_3$ series, and/or produces structural defects (e.g., anionic or cationic vacancies) which are generally associated with the physicochemical properties of the material (1–3). Much attention has been paid recently to perovskite-type oxides, after partial substitution of the A cation with elements having a valence state different from 3 +, as catalysts for hydrocarbon total oxidation due to their high activity and thermal stability (5–7). Less attention has been given to the effect of B cation substitution on catalytic properties (8, 9). Note that high-temperature applications, such as gas turbines, require materials stable to severe operating conditions (5, 10). Perovskite-like materials are indeed very resistant to high temperatures but often their limit in catalysis is represented by low values of surface area, if they are synthesized at high temperature (> 1373 K) using a solid-state reaction, starting from the component oxides. In this case the specific surface area is less than 5 $m^2\ g^{-1}$. To improve the catalytic activity it is thus necessary to produce such materials with larger surface areas using suitable precursors which may, under mild heat treatment, give the desired catalysts.

Among the oxidic perovskites, those containing lanthanum and manganese have received much attention in both fundamental and applied science since they apparently constitute the only system, in the lanthanum–transition metal perovskites, that exhibits, depending on the preparation conditions (temperature and atmosphere), a wide range of oxidative nonstoichiometry with strong modifications in their physicochemical properties.

For stoichiometric $LaMnO_3$ a reducing or inert atmosphere and a high temperature of preparation are necessary to preserve the Mn(III) oxidation state. At room temperature pure $LaMnO_3$ has a distorted orthorhombic (a = 5.537 Å, b = 5.743 Å, c = 7.695 Å) perovskite structure as a consequence of the Jahn–Teller distortion of the oxide octahedron around the d^4 Mn(III) ion (11). Elemans *et al.* studied $LaMnO_3$ by powder neutron diffraction and found that this compound has no La, Mn, or O vacancies or any other defect within the structure, and that three different Mn–O distances (1.905 Å, 1.959 Å, 2.187 Å; average 2.017 Å) are found by structure refinement, thus confirming the MnO_6 octahedral distortion (11). Goldschmidt's tolerance factor, t, is 0.96 for $LaMnO_3$ if the ionic radii from Shannon are taken into account (12). For $t < 1$, as in the case of $LaMnO_3$, the orthorhombic distortion from the ideal cubic structure of perovskite has indeed been predicted (4). Pure $LaMnO_3$ is antiferromagnetic with a Neel point T_N = 90 K and a magnetic moment $\mu = 5.0\ \mu_B$ (13), in agreement with the spin-only value ($\mu = 4.9\ \mu_B$).

When La–Mn oxide perovskite is prepared in air, several oxidized nonstoichiometric $LaMnO_{3+\delta}$ compounds, with Mn(III) and Mn(IV) ions present in the same structure, are obtained (11, 14–17). By setting the valence state of La to 3 +, it follows that (to preserve charge neutrality) for each value of δ, an equivalent amount (2δ) of Mn(III) should oxidize to Mn(IV). Since the oxidation of some Mn(III) to Mn(IV) reduces the Jahn–Teller distortion caused by the d^4 Mn(III) ion, a smaller deviation from the ideal cubic symmetry occurs so that the symmetry changes from orthorhombic (found in stoichiometric $LaMnO_3$) to primitive rhombohedral (or nonprimitive hexagonal) for a Mn(IV) concentration greater than 21% ($LaMnO_{3.105}$) (14–17). The cell volume per formula unit and the average Mn–O distance (2.0 Å) of the $LaMnO_{3+\delta}$ compounds were found to decrease with increasing Mn oxidation.

For nonstoichiometric oxidized $ABO_{3+\delta}$ perovskites at least three different models can be suggested: (a) incorporation of oxygen into the lattice as interstitial oxygen ions in sites of low electrostatic potential (this model is hardly likely since the ABO_3 perovskite structure consists of a close-packed AO_3 lattice with B cations in the O_6 octahedral sites), (b) vacancies on both A and B cation sites to leave a perfect oxide sublattice, (c) vacancies only on the A sites (B cation nonstoichiometry is less common since in the electrostatic model the B cations are much smaller and thus have a higher charge density than the A cations). In the last case migration of A cations to complete the B cation sublattice should occur. Note that for models (b) and (c) the notation $ABO_{3+\delta}$ is somewhat misleading, but it is commonly used. For model (b) with equal amounts of A and B vacancies, the notation $ABO_{3+\delta}$ normalized to three oxygens as expected for the perovskite structure becomes $A_{1-y}B_{1-y}O_3$, where $y = \delta/(3 + \delta)$.

Tofield and Scott (15) have proved by powder neutron diffraction that for the sample $LaMnO_{3.12}$, with a primitive rhombohedral cell, the nonstoichiometry involves La and Mn vacancies (La vacancies = 0.06, Mn vacancies = 0.02) rather than interstitial oxygens. Since the Mn(III)/Mn(IV) ratio in $LaMnO_{3.12}$, determined by redox titration, was 3.17, it followed that the formula normalized to three oxygens is $La_{0.94}Mn(III)_{0.745}Mn(IV)_{0.235}O_3$. In $LaMnO_{3.12}$ the Mn–O distance (1.965 ± 0.003 Å) is much lower than that observed by Elemans *et al.* in the stoichiometric $LaMnO_3$ (average value 2.017 Å) (11).

Van Roosmalen *et al.*, examined another nonstoichiometric $LaMnO_{3+\delta}$ sample by powder neutron diffraction, electron diffraction, high-resolution transmission electron

microscopy, and chemical analysis (16). Their results have shown that (a) no interstitial oxygen ions were present within the structure, (b) equal amounts (0.05) of La and Mn vacancies were present, and (c) no defect clustering or crystallographic shear occurred. The La/Mn ratio was 1.00 ± 0.001, and the Mn(III)/Mn(IV) ratio, as found by redox titration, was 2.17 ± 0.001, so in the $ABO_{3+\delta}$ notation the formula of the sample is $LaMnO_{3.158}$, whereas the formula normalized to three oxygens is $La_{0.95}Mn(III)_{0.65}Mn(IV)_{0.30}O_3$.

$LaCoO_3$ and its substituted $La_{1-x}Sr_xCoO_3$ and $LaCo_{1-x}Mn_xO_3$ parent perovskites have been studied for their magnetic and semiconducting properties (18–23). $LaCoO_3$ has a primitive rhombohedral (or nonprimitive hexagonal) perovskite structure. Goldschmidt's tolerance factor, t, is equal to 0.97 for $LaCoO_3$ if the ionic radii from Shannon are taken into account (12). $LaCoO_3$ itself is a p-type semiconductor. It is antiferromagnetic with an extrapolated paramagnetic Curie temperature $\theta < -200$ K and an effective magnetic moment $\mu = 3.4\ \mu_B$ (18). $LaCoO_3$ contains a mixture of d^6 trivalent paramagnetic Co^{3+} ($t_{2g}^4 e_g^2$ configuration with four unpaired electrons) and diamagnetic Co^{III} ($t_{2g}^6 e_g^0$ configuration) ions. Jia *et al.* (20) have shown that in $LaCo_{0.9}Mn_{0.1}O_3$ the presence of the paramagnetic trivalent Co^{3+} ion is due to the thermal excitation of the diamagnetic Co^{III} ion, the amount of Co^{3+} thus increasing with the increase in temperature. The calculated activation energy E from the Co^{III} ground state to the Co^{3+} excited state for the thermodynamic equilibrium $Co^{III} \Leftrightarrow Co^{3+}$ [$K = X(Co^{3+})/X(Co^{III}) = e^{-E/kT}$, where $X(Co^{III})$ and $X(Co^{3+})$ are the relative contents of the low-spin-state Co^{III} ion and the high-spin-state Co^{3+} ion] is equal to 0.006 eV in $LaCo_{0.9}Mn_{0.1}O_3$ (20). Slightly higher values for the activation energy from Co^{III} to Co^{3+} have been estimated in $LaCoO_3$ by Jonker ($E = 0.01$ eV) (18) and by Bhide *et al.* ($E = 0.02$ eV) (21). Note that in the great majority of inorganic materials trivalent cobalt is present in the low-spin Co^{III} state, the only exceptions being, to our knowledge, $LaCoO_3$ (and related cobalt containing perovskites) and A_3CoF_6 (A = alkali metals) (24), where the high-spin Co^{3+} state has been found.

In the light of the interesting physicochemical and catalytic properties disclosed by the manganese- and cobalt-containing lanthanum oxidic perovskites work has been undertaken by us with the aim of preparing high-surface-area $LaM_{1-x}Cu_xO_3$ (M = Mn or Co) perovskites by citrate precursors, to study the effect of copper on the structural properties of the perovskites and to investigate their redox properties as well as their catalytic activity toward methane combustion. In this paper the main solid-state physicochemical properties of the $LaMn_{1-x}Cu_xO_3$ and $LaCo_{1-x}Cu_xO_3$ systems are reported. Copper has been chosen as a substitute agent for manganese and for cobalt due to its stable Cu^{2+} valence state under the preparation conditions used by us.

EXPERIMENTAL

La, Mn (or Co), and Cu nitrates were mixed together in suitable proportions to give a concentrated solution. Citric acid was then proportionally added to the metal solution to have the same amounts of equivalents. The solution was evaporated at 333–363 K to produce a viscous syrup. The product was then heated at 383 K for 15 h, and evolution of brown smoke was observed. After grinding, the sample was heated very slowly from 383 to 453 to produce a vitreous solid (in this step of calcination a violent decomposition around 443 K, accompanied by brown smoke and NO_x gas evolution, was observed). The product was ground and fired at 573 K for 1 h. The sample was then reground and calcined for 5 h each at 823, 923, and 1073 K. For SEM and TEM investigations some samples calcined also at 1273 K were used. The La–Mn oxide sample was also fired in N_2 for 5 h at 1073 K. To gather information on their thermal stability some samples were also fired at 1373 and 1523 K.

The thermal behavior of the precursors was determined with a Stanton Redcroft STA-781 simultaneous TGA–DTA apparatus (Pt crucibles, Pt–Pt/Rh thermocouples, heating rate of 10 K min^{-1}), 20–30 mg of sample being employed for the runs. To avoid equipment damage due to the violent decomposition of the material observed in the range 383–453 K, the samples were preheated at 573 K before thermal analysis.

Chemical composition was determined by atomic absorption for Mn, Co, and Cu content. The valence state of manganese and cobalt was determined by dissolving the samples in a known excess of a ferrous sulfate standard solution and by titrating with potassium permanganate the excess of Fe(II). The titration was performed twice for each sample with the reproducibility of results always within 2%.

Phase analysis, lattice parameters, and particle size determination were performed by X-ray powder diffraction (XRPD) using a Philips PW 1029 diffractometer with Ni-filtered Cu$K\alpha$ radiation. Lattice parameters were calculated using the program UNITCELL method of T. J. B. Holland and SAT Redfern 1995. Particle sizes (D) were evaluated by means of the Scherrer equation $D = K\lambda/\beta\cos\theta$ after Warren's correction for instrumental broadening (25). K is a constant equal to 0.9; λ the wavelength of the X-ray used; β the effective linewidth of the X-ray reflection under observation, calculated by the expression $\beta^2 = B^2 - b^2$ [where B is the full width at half-maximum (FWHM), b the instrumental broadening determined through the FWHM of the X-ray reflection at $2\theta \approx 28^\circ$ of SiO_2 having particles larger than 1000 Å]; θ the diffraction angle of the (*102*) considered X-ray reflection ($2\theta_{102} \approx 23^\circ$).

BET surface areas (SA_{BET}) of the materials calcined at 923 and 1073 K were measured by N_2 adsorption at 77 K.

Surface area values were also calculated starting from particle sizes using the expression $SA_{calc} = 30{,}000/rd$, where

r is the radius of crystallites (supposed spherical) and is deduced from the crystallite sizes (D) measured by means of X-ray line broadening ($r = D/2$), and d is the X-ray density defined as $d = MZ/VN$, where M is the molar mass of the formula unit, Z the number of formula units per unit cell, V the measured unit cell volume, and N the Avogadro constant.

Mn, Co, and Cu K-edge X-ray absorption spectra (XAS) have been collected on 923 K calcined $LaMn_{1-x}Cu_xO_3$ samples with $x = 0.0$, 0.2, 0.4, 0.6, 1.0, on 923 K calcined $LaCo_{1-x}Cu_xO_3$ specimens with $x = 0.0$, 0.2, and 0.4, and on the reference compounds (CuO, MnO_2, Co_3O_4). Measurements have been performed at ESRF, GILDA beamline (Grenoble), by using a Si(311) double-crystal monochromator, at room temperature in the transmission and fluorescence modes. Samples have been deposited on Millipore membranes. X-ray spectra have been analyzed using the suite of programs by A. Michalowicz (LURE, Universitè Paris-sud).

SEM and TEM patterns were taken at the Laboratory of Professor R. J. Tilley, University of Cardiff, United Kingdom. A Jeol 35 CF microscope equipped with a LINK 860-2 system for analysis was used for SEM experiments, and Jeol 200 CX equipment was employed for TEM analysis.

Magnetic susceptibilities were measured by the Gouy method over the temperature range 100–300 K and at different magnetic field strengths. Correction was made for the diamagnetism of the samples.

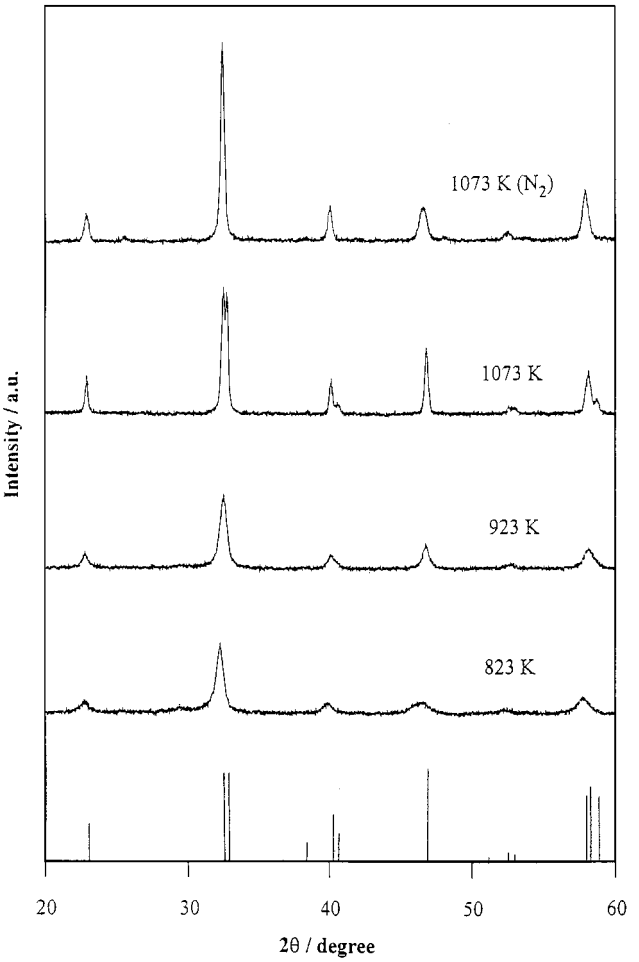

FIG. 1. Powder X-ray diffraction patterns for $LaMnO_3$ heated in air at 823, 923, and 1073 K, and in N_2 at 1073 K. X-ray lines belonging to $LaMnO_{3.15}$ (27a) are given at the bottom.

RESULTS AND DISCUSSION

For the sake of clarity the results for the two systems studied are presented and discussed separately.

1. $LaMn_{1-x}Cu_xO_3$

As stated under Experimental, the calcination of the precursors gave rise to a violent decomposition, accompanied by brown smoke, around 443 K. To avoid damage to the thermal equipment the samples were then precalcined above this temperature before testing for thermal analysis. The thermograms (not reported here) were similar for all precursors, independently of the manganese–copper composition. They showed two weight losses. The first, associated with a strong exothermic peak, starts around 573 K and ends around 823 K. This loss can be associated with the release of a great amount of CO_2 from the citrate. In the range 853–953 K, another smaller weight loss, associated with the release of residual CO_2 and NO_x, was observed.

The thermograms show a behavior similar to that reported by Taguchi *et al.*, for a citrate–nitrate gel obtained, as in our case, by adding the same equivalents of citric acid and metal nitrates (26). Note that the gel studied by Taguchi *et al.*, has been considered by thermal analysis and IR measurement to be $LaMn(C_6H_5O_7)(NO_3)_3$.

The calcination of the precursors was performed at 823, 923, and 1073 K. However, the samples calcined at 1073 K were investigated in more detail. For SEM and TEM investigations some samples calcined at 1273 K were used. Figure 1 shows the diffractograms for the La–Mn sample heated in air at 823, 923, and 1073 K and fired in N_2 at 1073 K.

Phase analysis revealed (see Fig. 2 for the samples calcined at 1073 K) the presence of a single perovskite phase with primitive rhombohedral cell [nonprimitive hexagonal cell (27a)] up to $x = 0.6$. However, for the compositions $x = 0.4$ and $x = 0.6$ the twin peaks (110)–(104) at $2\theta \approx 33^\circ$, (202)–(006) at $2\theta \approx 40^\circ$, (212)–(116) at $2\theta \approx 53^\circ$, and (301)–(117) at $2\theta \approx 58^\circ$ coalesce to single peaks. This indicates that the lattice tends to a higher symmetry as x increases. Note that the same behavior has been observed in

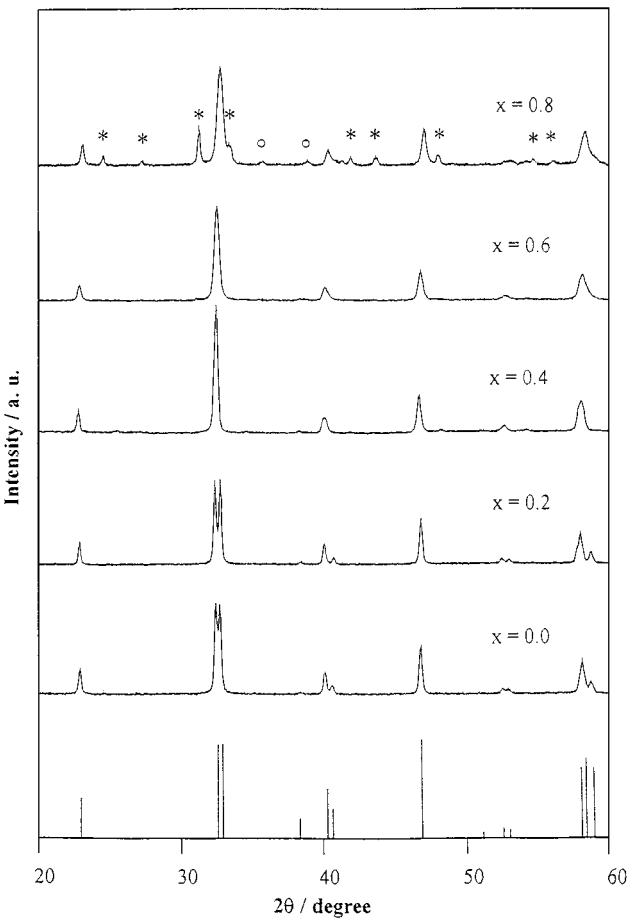

FIG. 2. Powder X-ray diffraction patterns for $LaMn_{1-x}Cu_xO_3$ calcined at 1073 K. X-ray lines belonging to $LaMnO_{3.15}$ (27a) are given at the bottom. Asterisks and circles for La_2CuO_4 (27b) and for CuO (27c), respectively, are reported.

$LaMnO_3$ treated in N_2 at 1073 K (see Fig. 1), and in the $La_{1-x}Sr_xCoO_3$ system (28–30). For $x = 0.8$ the strongest X-ray lines belonging to La_2CuO_4 (27b) and CuO (27c) were detected (Fig. 2) in addition to those of perovskite. For $x = 1.0$ the only phases present are CuO and La_2CuO_4. It may thus be inferred that, as already found by Rojas *et al.* (8), the substitution of manganese by copper totally preserves, up to $x = 0.6$, the perovskite structure. Only the results for samples having perovskite as a unique phase (up to $x = 0.6$) are discussed in more detail.

As pointed out by Tofield and Scott (15) and by van Roosmalen *et al.* (16), in La–Mn oxide perovskite there is no interstitial oxygen excess to compensate the higher charge of Mn(IV), the defect chemistry being thus given by vacancies on both *A* and *B* cation sites [in equal amounts, according to van Roosmalen *et al.* (16)]. This implies that the $ABO_{3+\delta}$ notation commonly used for perovskite-type compounds with oxidative nonstoichiometry should really be written in the normalized to three oxygens formula, and on the basis of *A* and *B* vacancies in equal amounts, as $A_{1-y}B_{1-y}O_3$, where $y = \delta/(3 + \delta)$.

Redox titration has shown that in the La–Mn perovskite ($x = 0.0$) there is a substantial fraction of manganese as Mn(IV) (35%, see Table 1), which reaches 58% in the sample with $x = 0.2$, 68% for $x = 0.4$, and 100% for $x = 0.6$. Thus, in agreement with the results of Tofield and Scott (15) and van Roosmalen *et al.* (16), also in our case the La–Mn perovskite can be regarded as a nonstoichiometric oxidized $LaMnO_{3+\delta}$ compound. On substitution of manganese by copper the charge neutrality is realized by further manganese oxidation. At high copper content [$x = 0.6$, 100% of Mn(IV)] the perovskite stoichiometry is achieved by the presence of oxygen vacancies. For $x > 0.6$, oxygen vacancies become so high that the perovskite structure was no longer stable, and La_2CuO_4 and CuO were formed together with a remaining fraction of Cu–Mn perovskite (see Fig. 2 for the sample with $x = 0.8$).

By taking into account the experimental Mn(III), Mn(IV), and copper contents (see Table 1), the following oxidative nonstoichiometric formulas were derived:

for $x = 0.0$, $LaMn(III)_{0.65}Mn(IV)_{0.35}O_{3.175}$;

for $x = 0.2$, $LaMn(III)_{0.34}Mn(IV)_{0.46}Cu_{0.2}O_{3.14}$;

for $x = 0.4$, $LaMn(III)_{0.19}Mn(IV)_{0.41}Cu_{0.4}O_3$;

for $x = 0.6$, $LaMn(IV)_{0.4}Cu_{0.6}O_{2.9}$.

By normalizing to the three-oxygen formula and supposing, as found by van Roosmalen *et al.* (16), the presence of an equal amounts of cation vacancies in the *A* and *B* sites, the following defective perovskites may be obtained:

for $x = 0.0$, $La_{0.94}Mn(III)_{0.61}Mn(IV)_{0.33}O_3$;

for $x = 0.2$, $La_{0.95}Mn(III)_{0.32}Mn(IV)_{0.44}Cu_{0.19}O_3$;

for $x = 0.4$, $LaMn(III)_{0.19}Mn(IV)_{0.41}Cu_{0.4}O_3$;

for $x = 0.6$, La $Mn(IV)_{0.4}Cu_{0.6}O_{2.9}$.

From the above formulation it is deduced that (i) La–Mn perovskite is a cation defective material, (ii) the numbers of cation vacancies in the *A* and *B* sites decrease for $x = 0.2$, (iii) for $x = 0.4$ the material does not show any defect chemistry, and (iv) oxygen vacancies are present in the structure for $x = 0.6$.

The stoichiometry of the compounds was confirmed by temperature-programmed reduction (see Part II). The samples after TPR were analyzed by XRD and found to contain only La_2O_3, $La(OH)_3$, MnO, and Cu^0 for the $LaMn_{1-x}Cu_xO_3$ solid solutions, and La_2O_3, $La(OH)_3$, and MnO in the case of $LaMnO_3$.

From the X-ray spectra of the samples calcined at 1073 K (more crystalline materials with very straight lines) the unit

TABLE 1
$LaMn_{1-x}Cu_xO_{3+\delta}$ Samples

	$x = 0$	$x = 0.2$	$x = 0.4$	$x = 0.6$
Mn_{exp} (%)	20.9	17.5	13.6	9.2
Mn_{nom} (%)	22.7	18.0	13.4	8.9
$Mn(III)/Mn_{tot}$	0.65	0.42	0.32	
$Mn(IV)/Mn_{tot}$	0.35	0.58	0.68	1.00
Cu_{exp} (%)		5.6	10.0	15.5
Cu_{nom} (%)		5.2	10.4	15.4
D_{102} (Å)—923 K	430 (290)	500 (320)	500 (320)	390 (280)
D_{102} (Å)—1073 K	730 (370)	940 (400)	810 (380)	590 (340)
SA_{BET} 923 K	36	26	24	21
SA_{calc} 923 K	21	18	17	22
SA_{BET} 1073 K	22	19	14	20
SA_{calc} 1073 K	13	10	11	15
a	5.516	5.515	5.513	5.501
c	13.33	13.27	13.42	13.39
V	351.3	349.6	353.4	350.9
Cu–O (Å) (CN)		2.00 (6)	1.95 (6)	1.93 (4)
Mn–O (Å) (CN)	1.94 (6)	1.94 (6)	1.92 (6)	1.91 (6)
μ_{exp} (μ_B)	5.7	4.7	3.5	2.7
μ_{calc} (μ_B)	4.7	4.0	3.5	2.9
T_C (K)	160	95	60	45

Note. Percentage of total experimental and nominal manganese content (Mn_{exp}, Mn_{nom}); fraction of Mn(III) [$Mn(III)/Mn_{tot}$] and Mn(IV) [$Mn(IV)/Mn_{tot}$]; percentage of experimental and nominal copper content (Cu_{exp}, Cu_{nom}); crystallite size, D_{102} (Å), for samples calcined at 923 and 1073 K; BET surface area (SA_{BET}, $m^2\,g^{-1}$) and calculated surface area (SA_{calc}, $m^2\,g^{-1}$) for samples calcined at 923 and 1073 K; lattice parameters for the hexagonal unit cell [lattice parameters for $LaMnO_{3.15}$: $a = 5.523$, $c = 13.324$, $V = 351.9$ (27a)]; observed Me–O distance (Å) with coordination numbers in parentheses; experimental (μ_{exp}) and calculated (μ_{calc}) magnetic moment; Curies temperature (T_C).

cell parameters were evaluated, by indexing the reflections on the basis of the nonprimitive hexagonal (primitive rhomboheral) cell corresponding to $LaMnO_{3.15}$ (27a). The values of a, c, and V for the samples up to $x = 0.6$ are reported in Table 1. It can be seen that a decreases continuously with increasing x, whereas the variation of c and V with copper content has an irregular behavior. In the light of the $LaMn_{1-x}Cu_xO_3$ composition given above, the irregular behavior of the cell volume variation can now be understood. It should be pointed out that at least four factors influence the variation of V with x: (i) replacement of Mn(III) by Mn(IV) [ionic radii for octahedral Mn(III) and Mn(IV) equal to 0.645 and 0.53 Å, respectively (12)], (ii) replacement of manganese by copper [ionic radius for octahedral Cu(II) = 0.73 Å (12)], (iii) decrease of cation vacancies, (iv) presence of anion vacancies content at $x = 0.6$. Factors (i) and (ii) have definitely opposite effects on the cell volume, e.g., contraction of V for (i) and expansion of V for (ii), whereas it is rather hard to quantify the effects on lattice volume of factors (iii) and (iv). For each sample, therefore, several parameters should be taken into account to foresee and rationalize the behavior of the variation of V with x.

The EXAFS spectra (after Fourier filtering, backtransform, and fitting of the first coordination shell) provided Cu–O distances of 2.0, 1.95, and 1.93 Å for the $LaMn_{1-x}Cu_xO_3$ samples with $x = 0.2$, 0.4, and 0.6, respectively, and Mn–O distances varying from 1.94 to 1.91 Å with the increase in copper content (Table 1). The coordination number, given in parentheses in Table 1, is nearly 6, except for copper in the sample with $x = 0.6$ where 4 was found. The Debye–Waller factors are 0.075 ± 0.001 and 0.068 ± 0.004 for copper and manganese, respectively.

As for copper, it may be recalled that the Cu–O distance expected on the basis of the sum of the ionic radii [Cu(II) octahedrally coordinated = 0.73 Å, O^{2-} = 1.40 Å (12)] should be much higher (2.13 Å). The observed lower values may be explained by a D_{4h} distortion of the copper sites (a shortening of the four planar bonds and a lengthening of the apical ones in the CuO_6 octahedron) and/or by a prevailingly covalent character of the Cu–O bond, both effects resulting in a shorter average Cu–O bond length. The decrease in Cu–O distance with x may be justified by a higher polarization of oxygens toward copper due to the lower coordination number caused by oxygen vacancies. Considering the presence of oxygen vacancies in the sample with $x = 0.6$ it is not surprising to find for this compound a coordination number lower than 6 (e.g., C.N. = 4).

The value of the Mn–O distance (1.94 Å) found in the La–Mn perovskite ($x = 0.0$) nearly agrees with that found by Tofield and Scott (15) in $LaMnO_{3.12}$ (1.965 ± 0.003 Å) where a fraction of Mn(IV) in addition to Mn(III) was found, whereas it is much lower than that observed by Elemans *et al.*, in the stoichiometric $LaMnO_3$ (average value 2.017 Å) where only Mn(III) is present (11). The trend of the slight decrease in Mn–O distance with the increase in Cu content is due to the increase in Mn(IV) concentration. Note that the Mn–O distances expected from the sum of ionic radii are 2.045 and 1.93 Å for Mn(III)–O and Mn(IV)–O bond lengths, respectively (12).

Redox titration has shown that in the $LaMn_{1-x}Cu_xO_3$ samples the Mn(IV) content increases with increasing copper concentration, reaching 100% for $x = 0.6$. XANES analysis confirmed this trend. It is well established that an increase in the oxidation state of a given element results in a shift of the relative XANES first-derivative peak toward higher energies (31). The XANES first derivatives obtained over the Mn K edge of samples $x = 0.0$ and $x = 0.6$ are shown in Fig. 3. For comparison, the XANES first derivative of MnO_2 is also plotted in Fig. 3. The shift toward higher energy (≈ 1.6 eV) shown by the $x = 0.6$ sample with respect to the $x = 0.0$ sample suggests an increase in the oxidation state for manganese with increasing Cu content. Note that the same effect has been observed in the $Nd_{1-x}Ca_xMnO_3$ system where the substitution of Ca(II) for

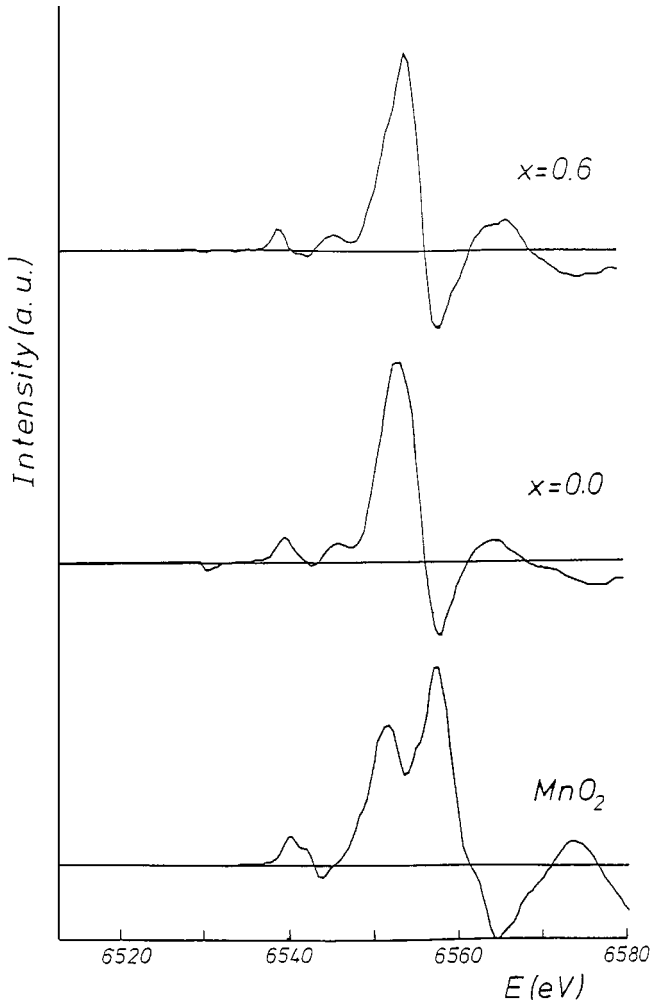

FIG. 3. First derivatives of the Mn *K*-edge XANES spectra for MnO_2 and $LaMn_{1-x}Cu_xO_3$ with $x = 0.0$ and $x = 0.6$.

Nd(III) induces an increase in the valence of Mn above 3 + (32).

The crystallite sizes (D_{102}), determined from the FWHM of the (102) diffraction peak using Scherrer's equation after Warren's correction of instrumental broadening (25) are reported in Table 1 for the samples calcined at 923 and 1073 K. Table 1 also reports, in parentheses, the crystallite sizes determined without correction of instrumental broadening. The crystallite sizes of the samples with $x = 0.0$, 0.2, and 0.4 are in the range 430–500 Å for those calcined at 923 K and in the range 730–940 Å for the samples calcined at 1073 K. The sample with $x = 0.6$ shows a much smaller value of *D*. This anomaly, as inferred by TEM and electron diffraction patterns (see later), may be due to the presence in this sample of extra phases such as CuO and La_2CuO_4 not detected by XRPD phase analysis. Note that the D_{102} values found by us for the perovskite with $x = 0.0$ (430 and 730 Å for samples calcined at 923 and 1073 K, respectively) are much higher than that determined by Tagushi *et al.* on a $LaMnO_{3+\delta}$ sample prepared with a $LaMn(C_6H_5O_7)(NO_3)_3$ citrate–nitrate gel with the same composition used by us and calcined in almost the same temperature range [from the gel with 0.007 mol of citric acid and 0.007 mol of metal nitrates: $D_{024} = 164$ Å for the sample calcined at 973 K (26)]. However, Taguchi *et al.* determined the crystallite sizes from the FWHM of an X-ray reflection [(024) at $2\theta \approx 46.8°$] different from that used by us [(102), at $2\theta = 23°$], and presumably no correction of instrumental broadening was applied in their work. If we consider the values of *D* reported in parentheses in Table 1 and determined by us without correction of instrumental broadening (290 and 370 Å for the $LaMnO_3$ sample calcined at 923 and 1073 K, respectively), the difference between our estimation and that of Taguchi *et al.* becomes smaller.

BET surface areas (SA_{BET}), reported in Table 1, are in the ranges 21–36 and 14–22 $m^2\,g^{-1}$ for the perovskite-like single phase $LaMn_{1-x}Cu_xO_3$ samples calcined at 923 and 1073 K, respectively. Also the surface areas (SA_{calc}) calculated on the basis of the radius of crystallite sizes and of the X-ray density ($d = 6.58$, 6.71, 6.91, and 6.97 $g\,cm^{-3}$ for $x = 0.0$, 0.2, 0.4, and 0.6, respectively) are reported in Table 1. Note that the values of SA_{BET} and SA_{calc} are of the same order of magnitude. The difference between SA_{BET} and SA_{calc} may be due to the fact that in the calculation of the surface area all particles were supposed to have a spherical shape, and this, as shown below by TEM, is not true in our samples.

SEM is an useful tool to obtain information on the morphology of samples so that two or more phases crystallized in different structures can be distinguished. However, for all samples calcined at 1073 K and for all the levels of magnification used by us (e.g., 2000, 10,000, and 20,000) the SEM patterns exhibited a not well-defined morphology (see Fig. 4 for $x = 0.4$ as example).

TEM associated with electron diffraction was used to reveal the possible presence of lattice defects in the structure and their distribution. The samples analyzed by TEM were those with $x = 0.0$ calcined at 1073 K and with $x = 0.6$ calcined at 1073 and 1273 K.

Figure 5 shows the TEM pattern for the sample with $x = 0.0$ calcined at 1073 K. Note that the crystals are almost regular hexagonal prisms with an average size of 0.08 μm (800 Å). The average size observed by TEM thus agrees with the value deduced from the FWHM of the diffraction peak ($D_{102} = 730$ Å). We have previously shown that the sample with $x = 0.0$ contains both Mn(III) and Mn(IV) and, by analogy with neutron diffraction studies (15, 16), equal amounts of cation vacancies on the *A* and *B* sites. If such defects would interact and form small clusters they should be recognized from TEM and a diffuse scattering in the electron diffraction patterns should appear. However, in any direction the crystals were orientated, no evidence of

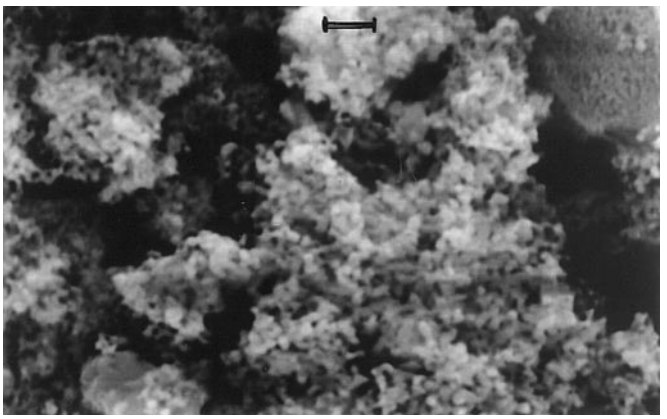

FIG. 4. SEM pattern (bar = 0.5 μm) for $LaMn_{1-x}Cu_xO_3$ with $x = 0.4$ calcined at 1073 K.

FIG. 6. TEM pattern (bar = 10 nm) for $LaMn_{1-x}Cu_xO_3$ with $x = 0.6$ calcined at 1073 K.

defects clustering was drawn out. This indicates, as found by van Roosmalen *et al.* in $LaMnO_{3.158}$ (16), that the cation vacancies in oxidized nonstoichiometric $LaMnO_{3+\delta}$ are randomly distributed. Moreover, the diffraction patterns confirmed that no interstitial oxygen is present since, in this case, evidence of microdomains, new phases, or crystallographic shear should be detected.

The results previously reported for the sample with $x = 0.6$ indicated that it contains only Mn(IV), and so, to preserve charge neutrality, $\approx 3.3\%$ of oxygen vacancies should be present in its structure. With respect to $LaMnO_3$ where the cation vacancies, due to strong electrostatic effects, cannot interact forming more extended defects, oxygen vancancies could lead to two types of interaction (33). In $ABO_{3-\delta}$ perovskites a single vacancy of the BO_6 octahedron can interact: (i) in a "linear" fashion with a vacancy situated on the other side of the octahedron, so forming linear clusters *B*–O–*B*–O–*B*–O (in this case the coordination of the *B* ion will change to square-planar), or (ii) in a "stepwise" model with a neighbor vacancy, so the coordination of *B* will change to tetragonal. The TEM pattern for the sample with $x = 0.6$ calcined at 1073 K, reported in Fig. 6, shows that the lattice structure of some crystals is strongly perturbed and not highly regular. With respect to the sample with $x = 0.0$ (Fig. 5), the material appears not homogeneous: the same crystal reveals shadow areas which diffract the electronic motion in a different way (so-called "spotty crystals"). The TEM pattern, for the sample with $x = 0.6$ calcined at 1273 K for 48 h, shows (Fig. 7a) an incipient ordering of defects and some clustering. In the diffraction image (Fig. 7b) some extra reflections are visible, probably due to a doubling of the unit cell. It may thus be suggested that the perovskite structure also at 1073 K contains anionic vacancies which, by firing the sample at higher temperature, interact to form more ordered and extended aggregates. On the other hand, the TEM pattern could indicate the incipient formation at 1273 K of extra phases such as CuO and La_2CuO_4 (not detected by XRD). The presence of small quantities of these oxides could be responsible for the irregular feature of the crystal lattices analyzed by TEM and for the diffuse scattering of the diffraction image.

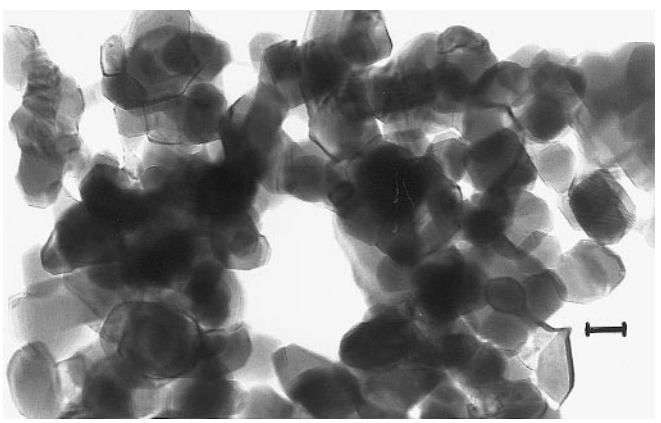

FIG. 5. TEM pattern (bar = 50 nm) for $LaMn_{1-x}Cu_xO_3$ with $x = 0.0$ calcined at 1073.

We finally discuss the magnetic properties of the $LaMn_{1-x}Cu_xO_3$ samples. Figure 8 shows the inverse atomic susceptibility, $1/\chi_{at}$ versus T, for the samples calcined at 1073 K. Note that the samples with $x = 0.0$ and $x = 0.2$ do not show a linear behavior of $1/\chi_{at}$ for all ranges of temperature. All samples exhibit a ferromagnetic behavior that decreases with increasing Cu content. The extrapolated Curie points, T_C, and the magnetic moments, μ, were derived from the straight parts of the $1/\chi_{at}$–T plots (for the $x = 0.0$ and 0.2 samples, the higher-temperature region was chosen). The values of μ and T_C are reported in Table 1.

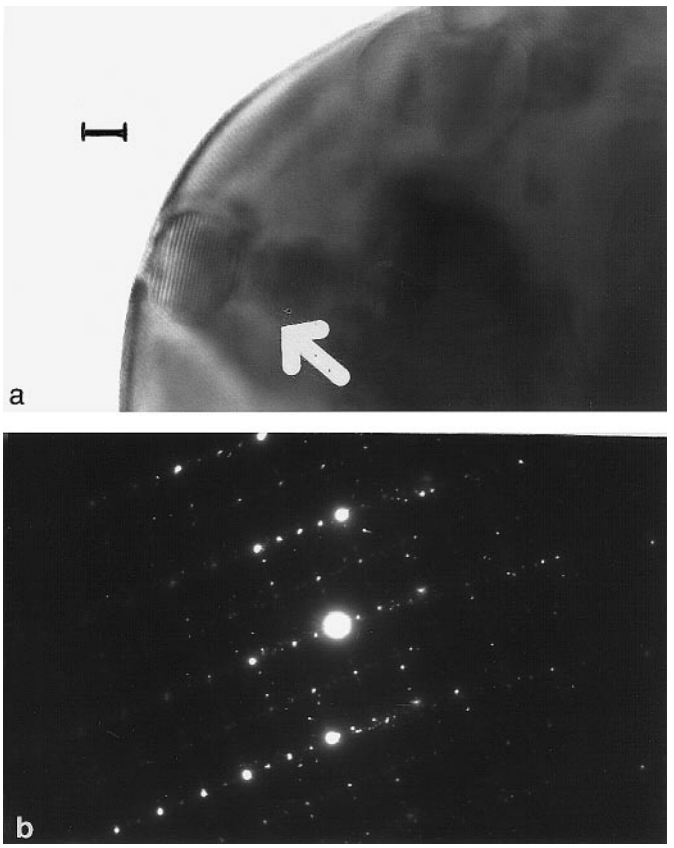

FIG. 7. $LaMn_{1-x}Cu_xO_3$ with $x = 0.6$ calcined at 1273 K: (a) TEM pattern (bar = 10 nm); (b) diffraction image.

some orbital contribution to the magnetic moment by the Mn(III) ion.

2. $LaCo_{1-x}Cu_xO_3$

The thermograms (not reported) were similar for all precursors, independently of the cobalt–copper composition, and resemble those obtained in the La–Mn–Cu system.

In Fig. 9 the diffractograms for $LaCoO_3$ calcined at 823, 923, and 1073 K are reported. $LaCoO_3$ calcined at 1523 K revealed the presence of only the perovskite phase (pattern not reported) so indicating its high thermostability.

Phase analysis revealed (see Figs. 10 and 11 for the $LaCo_{1-x}Cu_xO_3$ samples calcined at 923 and 1073 K, respectively) the presence of a single perovskite phase with primitive rhombohedral cell [nonprimitive hexagonal cell (27e)] up to $x = 0.2$. For $x = 0.4$ the appearance of the strongest X-ray line belonging to La_2CuO_4 (27b) indicated the presence of a very small quantity of this compound, in addition to the $LaCo_{1-x}Cu_xO_3$ perovskite phase. For $x = 0.6$ and $x = 0.8$ the amount of La_2CuO_4 increases and some CuO (27c) is also formed. For $x = 1.0$ the only phases present are La_2CuO_4 and CuO. A comparison of Figs. 10 and 11 shows, however, that at 923 K the $LaCo_{1-x}Cu_xO_3$ perovskite phase is already in a well-crystallized form, whereas La_2CuO_4 and CuO are less structured; a temperature of 1073 K must thus be achieved to produce more crystalline La_2CuO_4 and CuO phases. This indicates a greater ease of formation of the crystalline $LaCo_{1-x}$

The ferromagnetic behavior of oxidized nonstoichiometric La–Mn perovskite is indeed predicted by theory and is caused by the so-called "double-exchange" interaction between the Mn(III) and Mn(IV) ions (22). The T_C value for the sample with $x = 0.0$ (160 K) nearly agrees with that found (≈ 200 K) by Jonker (18). By progressive replacement of Mn with Cu in the $LaMn_{1-x}Cu_xO_3$ samples the Mn–O–Mn ferromagnetic interactions diminish and, as observed, T_C decreases. The magnetic moment for $LaMnO_3$ ($\mu = 5.7\ \mu_B$) is much higher than that expected from the spin-only values of the paramagnetic species present in the sample [Mn(III), Mn(IV)]. Note that for $LaMnO_3$ a rather high value ($\mu = 5.4\ \mu_B$) was also observed by Jonker (18). Taking into account the observed molar fraction of the paramagnetic ions [$X_{Mn(III)}$, $X_{Mn(IV)}$, $X_{Cu(II)}$], and the contribution to the paramagnetic moment of the molecule given by the spin-only value of each ion [$\mu_{Mn(III)} = 5.0\ \mu_B$, $\mu_{Mn(IV)} = 3.9\ \mu_B$, $\mu_{Cu(II)} = 1.7\ \mu_B$ (13)] the expected magnetic moments of each sample were calculated and reported in Table 1. It may be seen that, at least for the first range of compositions, the agreement between observed and calculated effective moments is not satisfactory. This could be due to

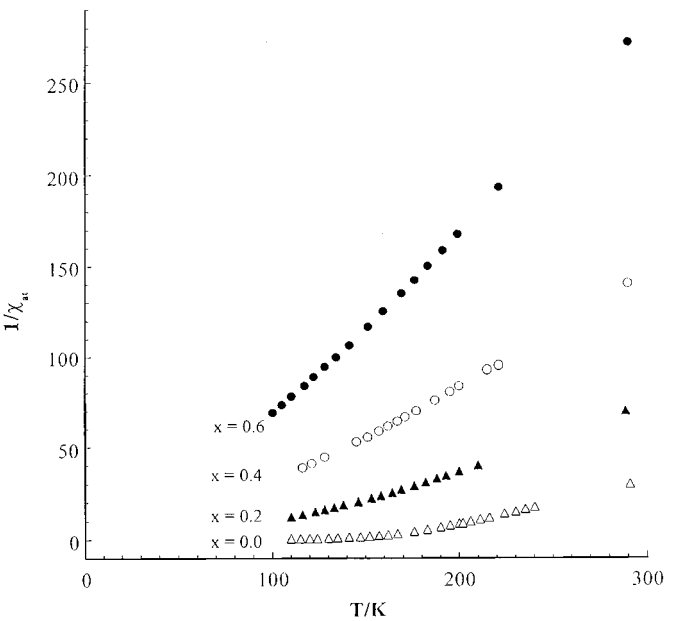

FIG. 8. Reciprocal atomic magnetic susceptibility $1/\chi_{at}$ versus T for $LaMn_{1-x}Cu_xO_3$ samples calcined at 1073 K.

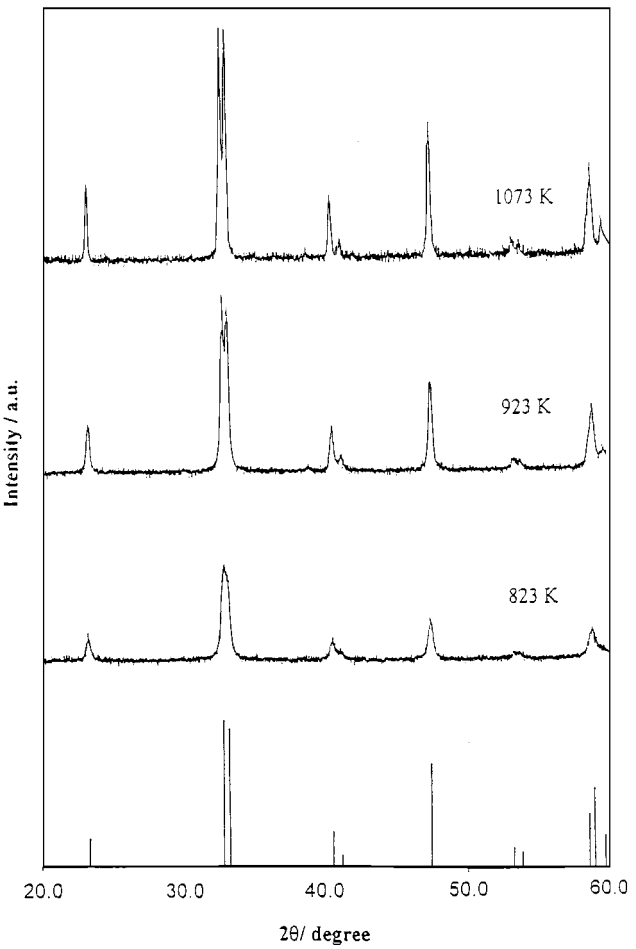

FIG. 9. Powder X-ray diffraction patterns for $LaCoO_3$ prepared by citrate precursors and calcined at 573, 823, 923, and 1073 K. X-ray lines belonging to $LaCoO_3$ (27a) are given at the bottom.

Cu_xO_3 perovskite phase with respect to La_2CuO_4 and CuO. Redox titration showed in all $LaCo_{1-x}Cu_xO_3$ samples the presence of cobalt in only the trivalent valence state, no Co^{4+} being detected.

Magnetic measurements displayed the following features:

i. A linear behavior of the inverse atomic susceptibility $1/\chi_{at}$ for all ranges of temperature was observed up to $x = 0.4$ (Fig. 12). The nonlinearity at lower temperatures of the $1/\chi_{at}$–T plots for $x \geq 0.6$ is probably due to the presence in the sample of larger quantities of La_2CuO_4 and CuO. In fact, the sample with $x = 1$, which contains only La_2CuO_4 and CuO, showed the most irregular behavior. Only the magnetic properties of the samples up to $x = 0.4$ are thus reported in Table 2.

ii. The intercepts to the axis of temperature of the $1/\chi_{at}$–T plots gave evidence of an antiferromagnetic behavior (Weiss temperature $\theta < 0$) which increases in modulus with increasing copper content.

iii. The magnetic moments, μ, decrease with increasing copper content.

By taking into account that in $LaCoO_3$ no paramagnetic Co^{4+} species was detected by redox titration and that La^{3+} and low-spin Co^{III} ($t_{2g}^6 e_g^0$ electronic configuration) are both diamagnetic, the paramagnetism observed in this sample must thus be due to the presence of a certain amount of high-spin Co^{3+} ($t_{2g}^4 e_g^2$ configuration with four unpaired electrons) species. For copper-containing samples the contribution to the paramagnetism of the molecule is of course given also by Cu^{2+} ($t_{2g}^6 e_g^3$ configuration with one unpaired electron).

The amount of Co^{3+} present in the $LaCo_{1-x}Cu_xO_3$ samples was evaluated from the observed values of μ. Because each magnetic metal ion can contribute to the total paramagnetic moment of the molecule, we can have

$$\mu^2 = \mu^2(Co^{3+}) \cdot X(Co^{3+}) + \mu^2(Cu^{2+}) \cdot X(Cu^{2+}), \quad [1]$$

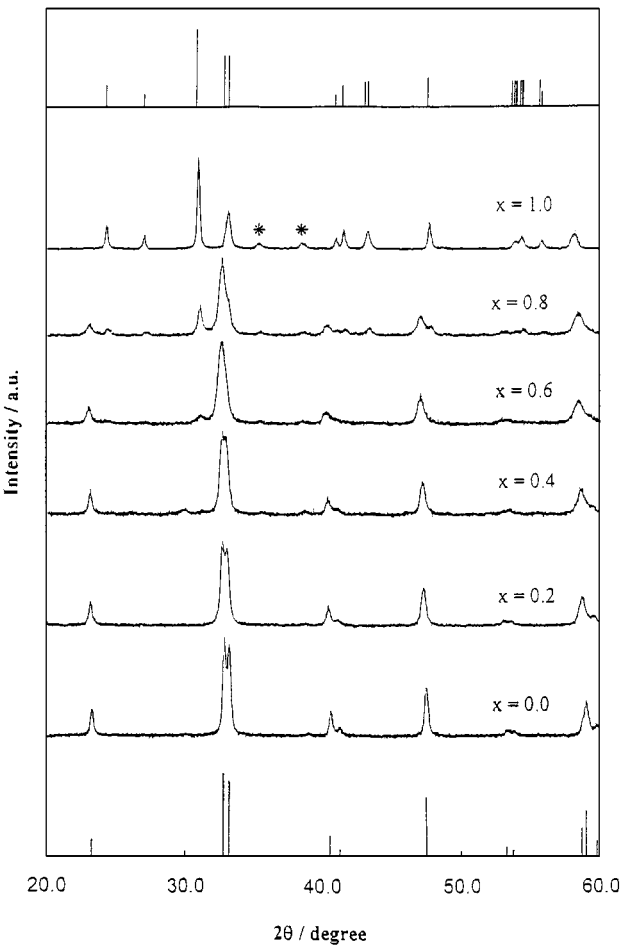

FIG. 10. Powder X-ray diffraction patterns for $LaCo_{1-x}Cu_xO_3$ calcined at 923 K. X-ray lines belonging to $LaCoO_3$ (27a) and to La_2CuO_4 (27b) are given at the bottom and the top, respectively. Asterisks for CuO (27c) are reported.

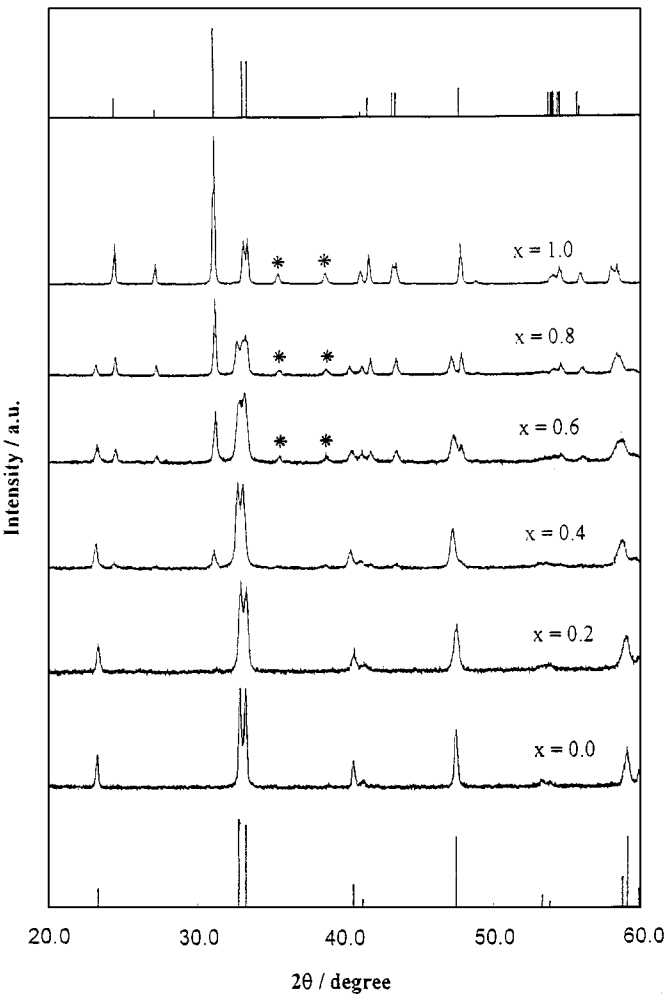

FIG. 11. Powder X-ray diffraction patterns for $LaCo_{1-x}Cu_xO_3$ calcined at 1073 K. X-ray lines belonging to $LaCoO_3$ (27a) and to La_2CuO_4 (27b) are given at the bottom and the top, respectively. Asterisks for CuO (27c) are reported.

where μ is the experimental value of the magnetic moment for each sample, $\mu(Co^{3+})$ and $\mu(Cu^{2+})$ are the expected spin-only values for Co^{3+} [$\mu(Co^{3+}) = 4.9\ \mu_B$] and for Cu^{2+} [$\mu(Cu^{2+}) = 1.7\ \mu_B$], and $X(Co^{3+})$ and $X(Cu^{2+})$ are the relative contents of the paramagnetic Co^{3+} and Cu^{2+} ions in the compounds, respectively.

The percentage of paramagnetic Co^{3+} species, reported in Table 2, was found to be around 34% for the samples up to $x = 0.4$, the remaining part of cobalt being of course constituted by the diamagnetic Co^{III} ions.

The presence of Co^{3+} in $LaCoO_3$ causes an antiferromagnetic superexchange coupling (22) through the strong hybridization of the Co^{3+}-e_g electrons with the oxygen $2p$ state. The substitution of cobalt by Cu^{2+} tends to increase the number of antiferromagnetically active cation–oxygen–cation interactions so that $|\theta|$ increases.

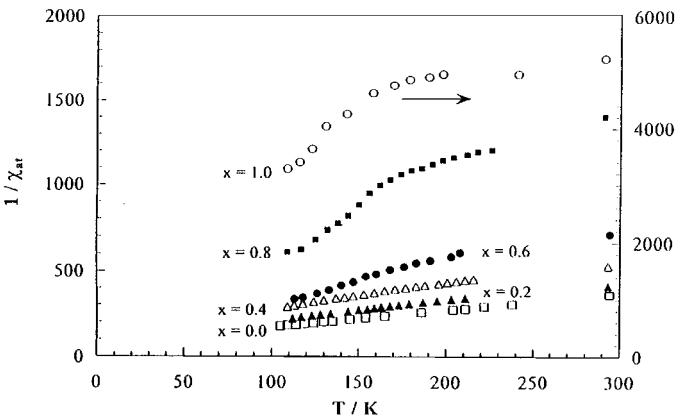

FIG. 12. Reciprocal atomic magnetic susceptibility $1/\chi_{at}$ versus T for $LaCo_{1-x}Cu_xO_3$ samples calcined at 1073 K.

The substitution of Cu^{2+} for cobalt leads to a positive charge defectivity which, in the lack of a corresponding cobalt oxidation to $4+$, is compensated by oxygen vacancies. The following chemical compositions may thus

TABLE 2
$LaCo_{1-x}Cu_xO_{3+\delta}$ Samples

	$x = 0$	$x = 0.2$	$x = 0.4$	$x = 0.6$	$x = 0.8$	$x = 1$
Cu_{exp} (%)		5.6	10.1	15.6	20.4	25.8
Cu_{nom} (%)		5.2	10.2	15.3	20.4	25.4
Co_{exp} (%)	24.3	19.3	14.3	9.5	4.8	
Co_{nom} (%)	24.0	19.1	14.3	9.5	4.7	
Co^{3+}/Co_{tot}	0.34	0.34	0.34			
Phases	P	P	P, (L)	P, L (T)	L, P (T)	L, T
D_{102}—923 K	440	390				
D_{102}—1073 K	990	990				
SA_{BET} 923 K	19	26	20	27	22	< 1
SA_{calc} 923 K	19	21	19			
SA_{BET} 1073 K	15	21	13	19	15	< 1
SA_{calc} 1073 K	8	8	8			
a	5.435	5.451	5.464			
c	13.07	13.09	13.15			
V	334.4	336.9	339.8			
Cu–O (CN)		1.98 (6)	1.96 (6)			
Co–O (CN)	1.92 (6)	1.91 (6)	1.92 (6)			
μ_{exp}	2.85	2.68	2.47			
$-\theta$	70	100	125			

Note. Percentage of experimental and nominal copper content (Cu_{exp}, Cu_{nom}); percentage of total experimental and nominal cobalt content (Co_{exp}, Co_{nom}); fraction of Co^{3+}/Co_{total}; phase detected by XRD; symbols for phases: P, perovskite; L, La_2CuO_4; T, tenorite; CuO, small amounts in parentheses; crystallite sizes, D_{102} (Å), for samples calcined at 923 K and 1073 K; BET surface areas (SA_{BET}, $m^2\,g^{-1}$) and calculated surface areas (SA_{calc}, $m^2\,g^{-1}$) for samples calcined at 923 and 1073 K; lattice parameters for the hexagonal unit cell [lattice parameters for $LaCoO_3$: $a = 5.441$ Å, $c = 13.088$ Å, $V = 335.55$ Å^3 (27e)]; observed Me–O distances (Å) with coordination numbers in parentheses; experimental (μ_{exp}) magnetic moments (μ_B); Weiss temperature (θ/K).

be suggested for the $LaCo_{1-x}Cu_xO_3$ samples up to $x = 0.4$:

(i) for $x = 0$: $LaCo^{3+}_{0.34}Co^{III}_{0.66}O_3$;

(ii) for $x = 0.2$: $LaCo^{3+}_{0.28}Co^{III}_{0.52}Cu_{0.2}O_{2.9}$;

(iii) for $x = 0.4$: $LaCo^{3+}_{0.21}Co^{III}_{0.39}Cu_{0.4}O_{2.8}$.

From the X-ray spectra of the $LaCo_{1-x}Cu_xO_3$ samples (up to $x = 0.4$) calcined at 1073 K the lattice parameters of the nonprimitive hexagonal (primitive rhombohedral) cell corresponding to $LaCoO_3$ (27e) were evaluated (Table 2). An increase in a, c, and V with an increase in copper was found. The lattice expansion is due to the replacement of cobalt by larger copper ions [ionic radius for octahedral $Co^{3+} = 0.61$ Å, for $Co^{III} = 0.545$ Å, for $Cu^{2+} = 0.73$ Å (12)].

The EXAFS spectra (after Fourier filtering, backtransform, and fitting of the first coordination shell) gave values for the Cu–O distances equal to 1.98 and 1.96 Å for the samples with $x = 0.2$ and 0.4, respectively, and around 1.92 Å for Co–O in all samples (Table 2). The coordination number, reported in parentheses in Table 2, is 6. The Debye–Waller factors are 0.070 ± 0.001 and 0.05 ± 0.02 for copper and cobalt, respectively.

The values of the Cu–O bond length (much lower than that expected on the basis of the sum of the ionic radii, 2.13 Å) can be explained also in this case, as in the $LaMn_{1-x}Cu_xO_3$ system, by the prevailingly covalent character of the Cu–O bond and/or by a D_{4h} distortion of the copper sites.

Also, the Co–O distance is lower than that expected on the basis of the sum of the ionic radii (Co^{3+}–O = 2.01 Å, Co^{III}–O = 1.945 Å), and a covalent contribution to the bond may be the cause of the observed difference.

XANES analysis confirmed the occurrence of the trivalent state for cobalt. The Co K-edge XANES first derivatives obtained for the samples with $x = 0.0$, 0.2, and 0.4 are shown in Fig. 13. For comparison the XANES first derivative of Co_3O_4 (containing Co^{2+} and Co^{3+}) is also plotted in Fig. 13. It may be seen that no change in the shape and position of the peaks occurs with the variation of x. The maximum of the derivative peak is for all samples at ≈ 7725 eV. Since the analysis of the peak derivative for Co_3O_4 showed the presence of three maxima at 7719, 7724, and 7729 eV, it may be inferred that cobalt in our samples cannot have an oxidation state greater than 3+.

The crystallite sizes (D_{102}) of $LaCoO_3$ and $LaCo_{0.8}Cu_{0.2}O_{2.9}$, determined from the FWHM of the (102) diffraction peak using Scherrer's equation after Warren's correction of instrumental broadening (25), are reported in Table 2. Their values are around 400 and 1000 Å for the samples calcined at 923 and 1073 K, respectively.

BET surface areas (SA_{BET}), reported in Table 2, are in the ranges 19–27 and 13–21 $m^2 g^{-1}$ for the samples calcined at 923 and at 1073 K, respectively. The surface areas (SA_{calc}) calculated for $LaCoO_3$ and $LaCo_{0.8}Cu_{0.2}O_{2.9}$ on the basis of the radius of crystallite sizes and the X-ray density ($d = 7.32$ and 7.25 g cm^{-3} for $x = 0.0$ and $x = 0.2$, respectively) are also reported in Table 2. Note that the values of SA_{BET} and SA_{calc} are similar for the samples calcined at 923 K, and of the same order of magnitude for those calcined at 1073 K. The difference between SA_{BET} and SA_{calc} in the latter case may be due to the fact that in the calculation of the surface area all particles were supposed to have a spherical shape, and this, as shown below by TEM, is not true in our samples.

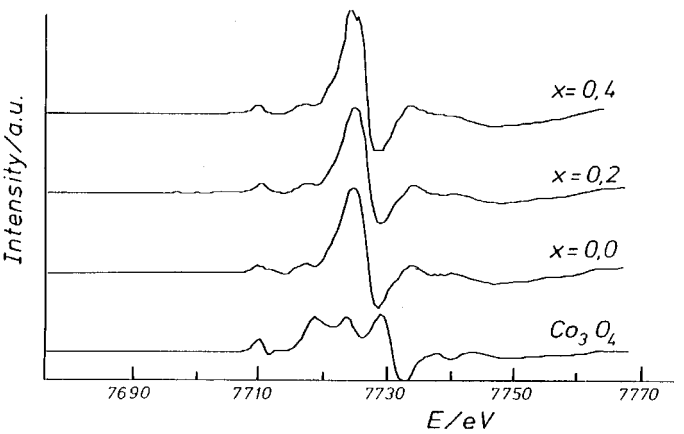

FIG. 13. First derivatives of the Co K-edge XANES spectra for Co_3O_4 and for the samples $LaCo_{1-x}Cu_xO_3$ with $x = 0.0$, 0.2, and 0.4, calcined at 923 K.

SEM patterns exhibited a not well-defined morphology for all samples calcined at 1073 K and for all the levels of magnification used by us (e.g., 2000, 10,000, and 20,000). Figure 14a shows an example for $x = 0.2$. However, the SEM pattern taken on the same sample calcined at 1273 K (Fig. 14b) revealed the presence of well-formed and -defined crystalline structures.

Figures 15a and 15b report the TEM patterns for the sample with $x = 0.2$ calcined at 1073 and at 1273 K, respectively. Figure 15a shows almost regular hexagonal prismatic crystals which are connected to form "linked structures." The pattern reveals the presence of some "spotty crystals" which could be interpreted as short-range ordered local defects. Neither planar defects nor high concentrations of other defects are visible. Note that the sample calcined at 1273 K revealed the same XRD pattern as that calcined at 1073 K. The TEM pattern of the 1273 K specimen (Fig. 15b) shows larger crystals with evidence of a larger amount of defective crystals and the presence of "planar faults." It may be suggested that at $T > 1073$ K the anionic vacancies present in this sample ($\approx 3.3\%$) interact to form more extended defects such as small clusters. The occurrence of "planar faults" could be due to the presence of

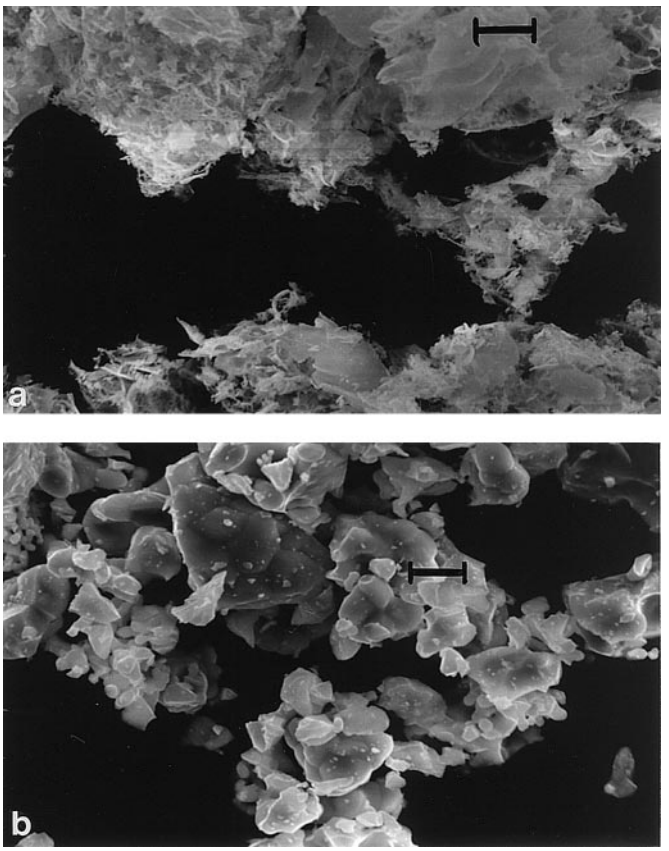

FIG. 14. SEM patterns (a) for the sample $LaCo_{1-x}Cu_xO_3$ with $x = 0.2$ calcined at 1073 K (bar = 3 μm) and (b) for the sample $LaCo_{1-x}Cu_xO_3$ with $x = 0.2$ calcined at 1273 K (bar = 3 μm).

randomly oriented layers of La_2CuO_4 not detected by X-ray diffraction.

CONCLUSION

The following conclusions can be drawn for the two series studied:

1. $LaMn_{1-x}Cu_xO_3$

i. $LaMn_{1-x}Cu_xO_3$ ($x = 0.0, 0.2, 0.4, 0.6, 0.8, 1.0$) are perovskite-like single phases up to $x = 0.6$. For $x = 0.8$ CuO and La_2CuO_4 phases are present in addition to perovskite. For $x = 1.0$ the material is formed by CuO and La_2CuO_4.

ii. Mn(IV) is found in all Mn-based perovskite samples, its fraction increasing with the increase in copper content.

iii. A ferromagnetic behavior, which decreases with the increase in x, is observed.

iv. Cation vacancies in the 12-coordinated A and octahedral B sites are suggested for the materials with $x = 0.0$ and 0.2. For $x = 0.4$ the perovskite is stoichiometric, whereas oxygen vacancies are present for $x = 0.6$.

v. No evidence of defect clustering is observed for the samples with $x = 0.0$ and 0.2. For the $LaMn_{0.4}Cu_{0.6}O_3$ sample a perturbation of the structure is revealed.

2. $LaCo_{1-x}Cu_xO_3$

i. $LaCo_{1-x}Cu_xO_3$ ($x = 0.0, 0.2, 0.4, 0.6, 0.8, 1.0$) are perovskite-like single phases up to $x = 0.2$. For $x = 0.4$ a very small amount of La_2CuO_4, in addition to perovskite, is present. For $x \geq 0.6$ massive formation of La_2CuO_4 and CuO, in addition to perovskite, is observed.

ii. Only trivalent cobalt, as a mixture of paramagnetic Co^{3+} and diamagnetic Co^{III}, is present in all samples. The Co^{3+} fraction is, at least up to $x = 0.4$, equal to ≈ 0.34.

iii. All materials are antiferromagnetic. The antiferromagnetism, associated with the superexchange coupling interaction, increases with the increase in x.

iv. $LaCoO_3$ is a stoichiometric perovskite. The substitution of cobalt by Cu^{2+} leads to a positive charge defectivity which is compensated by oxygen vacancies.

v. Short-range ordered local defects are present in samples calcined at 1073 K. A higher degree of defectivity and

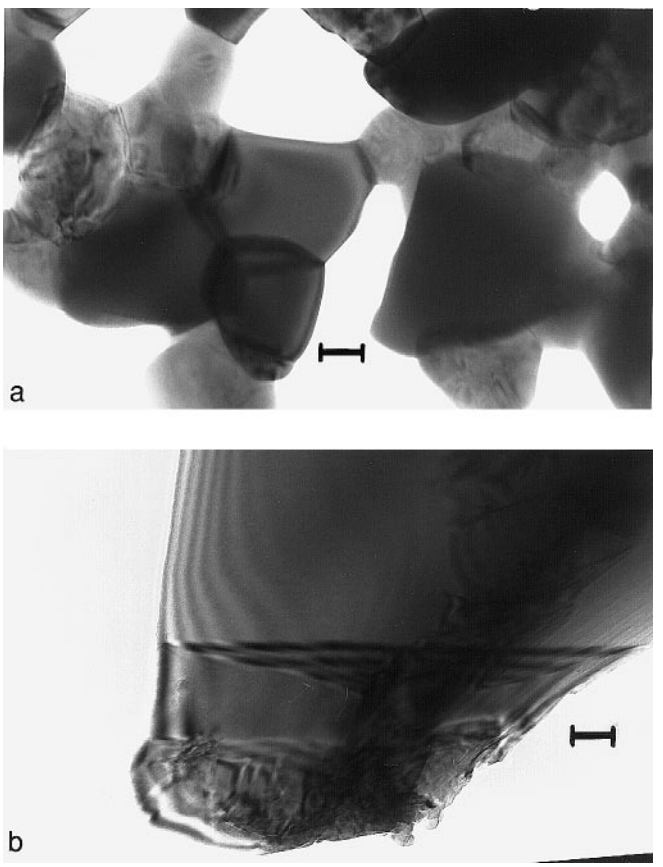

FIG. 15. TEM patterns (a) for the sample $LaCo_{1-x}Cu_xO_3$ with $x = 0.2$ calcined at 1073 K (bar = 50 nm) and (b) for the sample $LaCo_{1-x}Cu_xO_3$ with $x = 0.2$ calcined at 1273 K (bar = 10 nm).

"planar faults" are observed in copper-containing samples calcined at 1273 K.

ACKNOWLEDGMENTS

Thanks are extended to Professor R. J. Tilley, University of Cardiff, United Kingdom, for the use of SEM and TEM equipment and for the helpful discussions with M. Faticanti who was guest for 2 months in his laboratory. We also thank Mr. M. Inversi for the drawings.

REFERENCES

1. R. E. Newman, *in* "Structure–Property Relationship in Perovskite Electroceramics: Perovskite: A Structure of Great Interest to Geophysics and Material Science" (A. Navrotsky and D. J. Weidner, Eds.), American Geophysical Union, Washington, DC, 1989.
2. L. G. Tejuco and J. L. G. Fierro (Eds.), "Properties and Applications of Perovskite-Type Oxides." Marcel Dekker, New York, 1993.
3. R. J. H. Voorhoeve, D. W. Johnson, Jr., J. P. Remeika, and P. K. Gallagher, *Science* **195,** 827 (1977).
4. V. M. Goldschimdt, *Akad. Oslo. J. Mat. Natur.* **2,** 7 (1926).
5. H. Arai and M. Machida, *Catal. Today* **10,** 81 (1991).
6. L. G. Tejuca, J. L. G. Fierro, and J. M. D. Tascon, *Adv. Catal.* **36,** 237 (1989).
7. L. Marchetti and L. Forni, *Appl. Catal. B Environ.* **15,** 179 (1998).
8. M. L. Rojas, J. L. G. Fierro, L. G. Tejuca, and A. T. Bell, *J. Catal.* **124,** 41 (1990).
9. E. M. Vogel, D. W. Johnson, Jr., and P. K. Gallagher, *J. Am. Ceram. Soc.* **60,** 31 (1977).
10. K. Eguchi and H. Arai, *Catal. Today* **29,** 379 (1996).
11. J. B. A. A. Elemans, B. Van Laar, K. R. Van der Veen, and B. O. Loopstra, *J. Solid State Chem.* **3,** 238 (1971).
12. R. D. Shannon, *Acta Crystallogr. Sect. A* **32,** 751 (1976).
13. M. Schieber, *in* "Experimental Magnetochemistry," p. 265. North-Holland, Amsterdam, 1967.
14. A. Wold and R. J. Arnott, *J. Phys. Chem. Solids* **9,** 176 (1959).
15. B. C. Tofield and W. R. Scott, *J. Solid State Chem.* **10,** 183 (1974).
16. J. A. M. van Roosmalen, E. H. P. Cordfunke, R. B. Helmholdt, and H. W. Zandbergen, *J. Solid State Chem.* **110,** 100 (1994).
17. I. G. Krogh Andersen, E. Krogh Andersen, P. Norby, and E. Skou, *J. Solid State Chem.* **113,** 320 (1994).
18. G. H. Jonker, *J. Appl. Phys.* **37**(3), 1424 (1966).
19. G. H. Jonker and J. H. van Santen, *Physica* **29,** 120 (1953).
20. Y. Q. Jia, S. T. Liu, and Y. Wu, *J. Solid State Chem.* **113,** 215 (1994).
21. V. G. Bhide, D. S. Rajora, C. R. Rao, *Phys. Rev. B* **6,** 1021 (1972).
22. J. B. Goodenough, *in* "Magnetism and the Chemical Bond," p. 221. Wiley, New York, 1963.
23. M. Schieber, *in* "Experimental Magnetochemistry," p. 265. North-Holland, Amsterdam, 1967.
24. W. Klem, W. Brandt, and R. Hoppe, *Z. Anorg. Allg. Chem.* **308,** 179 (1961).
25. H. P. Klug and L. E. Alexander, *in* "X-ray Diffraction Procedures for Polycrystalline and Amorphous Materials." Wiley, London, 1962.
26. H. Taguchi, S. Matsu-ura, M. Nagao, T. Choso, and K. Tabata, *J. Solid State Chem.* **129,** 60 (1997).
27. "X-Ray Powder Data File," ASTM cards: (a) 32–484 for $LaMnO_{3.15}$; (b) 30–487 for La_2CuO_4; (c) 5–0661 for CuO; (d) 33–713 for $LaMnO_3$; (e) 25–1060 for $LaCoO_3$.
28. R. H. van Doom, J. Boejisma, and A. J. Burggraaf, *Powder Diffraction* **10,** 261 (1995).
29. J. E. ten Elshof and J. Boejisma, *Powder Diffraction* **11,** 28 (1996).
30. N. M. L. N. Closset, R. H. van Doom, and H. Kruidhof, *Powder Diffraction* **11,** 31 (1996).
31. A. Bianconi, *in* "X-ray Absorption: Principles, Applications, Techniques of EXAFS, SEXAFS and XANES" (D. C. Koningsberger and R. Prins, Eds.), p. 573. Wiley, New York, 1988.
32. R. S. Liu, J. B. Wu, C. Y. Chang, J. G. Lin, C. Y. Huang, J. M. Chen, and R. G. Liu, *J. Solid State Chem.* **125,** 112 (1996).
33. J. A. M. van Roosmalen and H. P. Cordfunke, *J. Solid State Chem.* **93,** 212 (1991).